Article

Quantum-limit Chern topological magnetism in $TbMn_6Sn_6$

https://doi.org/10.1038/s41586-020-2482-7

Received: 6 September 2019

Accepted: 14 April 2020

Published online: 22 July 2020

Check for updates

Jia-Xin Yin[1,15]✉, Wenlong Ma[2,15], Tyler A. Cochran[1,15], Xitong Xu[2,15], Songtian S. Zhang[1], Hung-Ju Tien[3], Nana Shumiya[1], Guangming Cheng[4], Kun Jiang[5], Biao Lian[6], Zhida Song[7], Guoqing Chang[1], Ilya Belopolski[1], Daniel Multer[1], Maksim Litskevich[1], Zi-Jia Cheng[1], Xian P. Yang[1], Bianca Swidler[1], Huibin Zhou[2], Hsin Lin[8], Titus Neupert[9], Ziqiang Wang[5], Nan Yao[4], Tay-Rong Chang[3,10,11], Shuang Jia[2,12,13]✉ & M. Zahid Hasan[1,14]✉

The quantum-level interplay between geometry, topology and correlation is at the forefront of fundamental physics[1–15]. Kagome magnets are predicted to support intrinsic Chern quantum phases owing to their unusual lattice geometry and breaking of time-reversal symmetry[14,15]. However, quantum materials hosting ideal spin–orbit-coupled kagome lattices with strong out-of-plane magnetization are lacking[16–21]. Here, using scanning tunnelling microscopy, we identify a new topological kagome magnet, $TbMn_6Sn_6$, that is close to satisfying these criteria. We visualize its effectively defect-free, purely manganese-based ferromagnetic kagome lattice with atomic resolution. Remarkably, its electronic state shows distinct Landau quantization on application of a magnetic field, and the quantized Landau fan structure features spin-polarized Dirac dispersion with a large Chern gap. We further demonstrate the bulk–boundary correspondence between the Chern gap and the topological edge state, as well as the Berry curvature field correspondence of Chern gapped Dirac fermions. Our results point to the realization of a quantum-limit Chern phase in $TbMn_6Sn_6$, and may enable the observation of topological quantum phenomena in the RMn_6Sn_6 (where R is a rare earth element) family with a variety of magnetic structures. Our visualization of the magnetic bulk–boundary–Berry correspondence covering real space and momentum space demonstrates a proof-of-principle method for revealing topological magnets.

The exploration of quantum topology under non-trivial lattice geometry and strong electron interaction is emerging as a new frontier in condensed-matter physics that not only has analogies with high-energy physics but also expands the range of quantum materials available for next-generation technology[1–15]. Recently, the transition-metal-based kagome magnets have attracted great attention, as they often show correlated topological band structures[7,8,16–20]. A kagome lattice, made of corner-sharing triangles, naturally has relativistic band crossings at the Brillouin zone corners (Fig. 1a). The inclusion of spin–orbit coupling and out-of-plane ferromagnetic ordering in the kagome lattice effectively realizes the spinless Haldane model by generating Chern gapped topological fermions[9,10,13–15] (Fig. 1b). However, direct experimental visualization of the phenomenon remains challenging owing to the existence of tin atoms in the kagome layer, the close stacking of the kagome lattices and the tendency to form in-plane magnetization for most kagome magnets[16–20]. Through intense research in this study, we find that $TbMn_6Sn_6$ is a key advance in quantum materials. Unlike other members of the kagome magnet family, it consists of segregated kagome layers formed purely by manganese atoms. More crucially, its kagome lattice uniquely features both an out-of-plane magnetization ground state and the largest coercivity (1.1 T) within the RMn_6Sn_6 family (Fig. 1c)[22–24]. Therefore, $TbMn_6Sn_6$ is a tantalizing system to search for the Chern gapped topological fermions.

$TbMn_6Sn_6$ has a layered crystal structure with space group *P6/mmm* and hexagonal lattice constants $a = 5.5$ Å and $c = 9.0$ Å. It consists of a manganese kagome layer with tin and terbium successively distributed in alternating layers stacked along the *c* axis. The material has a ferrimagnetic ground state (Curie temperature, $T_C = 423$ K), with a manganese moment of 2.4 Bohr magnetons (μ_B) ferromagnetically aligned along the *c* axis and a terbium moment of $8.6\mu_B$ anti-aligned along the *c* axis (Fig. 1d)[24]. We grew high-quality single crystals using a flux method. The $TbMn_6Sn_6$ crystal shows a well-defined magnetization

[1]Laboratory for Topological Quantum Matter and Advanced Spectroscopy (B7), Department of Physics, Princeton University, Princeton, NJ, USA. [2]International Center for Quantum Materials, School of Physics, Peking University, Beijing, China. [3]Department of Physics, National Cheng Kung University, Tainan, Taiwan. [4]Princeton Institute for Science and Technology of Materials, Princeton University, Princeton, NJ, USA. [5]Department of Physics, Boston College, Chestnut Hill, MA, USA. [6]Princeton Center for Theoretical Science, Princeton University, Princeton, NJ, USA. [7]Department of Physics, Princeton University, Princeton, NJ, USA. [8]Institute of Physics, Academia Sinica, Taipei, Taiwan. [9]Department of Physics, University of Zurich, Zurich, Switzerland. [10]Center for Quantum Frontiers of Research and Technology (QFort), Tainan, Taiwan. [11]Physics Division, National Center for Theoretical Sciences, Hsinchu, Taiwan. [12]CAS Center for Excellence in Topological Quantum Computation, University of Chinese Academy of Sciences, Beijing, China. [13]Beijing Academy of Quantum Information Sciences, Beijing, China. [14]Lawrence Berkeley National Laboratory, Berkeley, CA, USA. [15]These authors contributed equally: Jia-Xin Yin, Wenlong Ma, Tyler A. Cochran, Xitong Xu. ✉e-mail: jiaxiny@princeton.edu; gwljiashuang@pku.edu.cn; mzhasan@princeton.edu

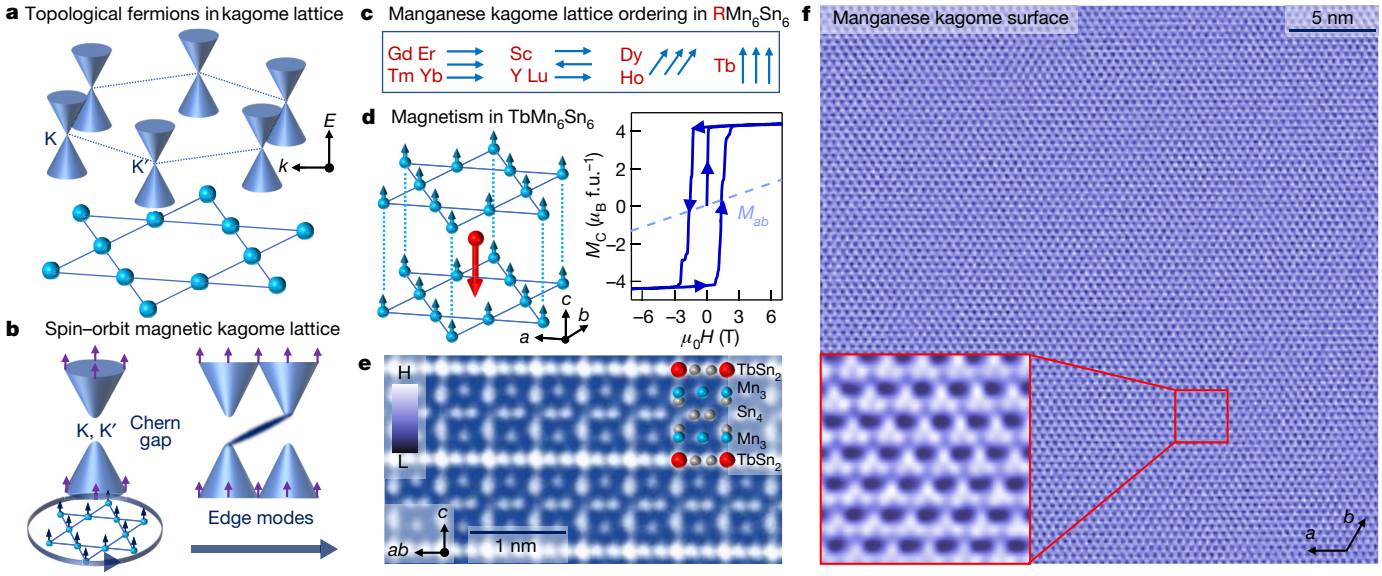

Fig. 1 | Atomic-scale visualization of the defect-free magnetic kagome lattice. a, Illustration of Dirac band crossings (hourglass cones) at the Brillouin zone (dashed lines) corners for a kagome lattice (spheres connected by solid lines). **b**, Left, illustration of spin-polarized Dirac fermions with a Chern gap (two separated cones with upward arrows indicating spin polarization) in the spin–orbit-coupled magnetic kagome lattice (spheres with upward arrows indicating ferromagnetism). Right, illustration of the edge mode (purple dark region between the tips of two cones) that arises within the Chern gap. **c**, Summary of the magnetic ground state of the manganese kagome lattice in the RMn_6Sn_6 family, including in-plane ferromagnetism (R = Gd, Er, Tm, Yb), in-plane antiferromagnetism (R = Sc, Y, Lu), canted ferromagnetism (R = Dy, Ho) and out-of-plane ferromagnetism (R = Tb). **d**, Magnetism in $TbMn_6Sn_6$, with the left image illustrating its magnetic structure of manganese (blue) and terbium (red) atoms, and the right image showing the out-of-plane (solid lines) and in-plane (dashed lines) magnetization curves taken at 4.2 K. 'f.u.' denotes the formula unit. **e**, Scanning transmission electron microscope image of $TbMn_6Sn_6$, showing the atomic interlayer stacking. H, high; L, low. **f**, Scanning tunnelling microscopy image of the manganese-terminating surface taken at 4.2 K. The inset shows a magnified image of the kagome lattice.

loop for the field applied along the *c* axis and no magnetization loop for the field applied within the *a*–*b* plane in Fig. 1d (right), confirming the strong out-of-plane magnetization. The side-plane map of the crystal measured by scanning transmission electron microscopy in Fig. 1e directly shows its atomic stacking sequence along the *c* axis. It can be seen that the interlayer distance between the TbSn layer and the manganese layer is the largest, and the crystal tends to cleave along this plane. By searching extensively over 50 cryogenically cleaved crystals with low-temperature ($T = 4.2$ K) scanning tunnelling microscopy, we were able to obtain a large atomically flat manganese kagome lattice, as shown in Fig. 1f. Its zoomed-in image, measured with a much lower junction resistance setup, directly reveals the manganese kagome atoms. Moreover, unlike topographies of the kagome lattice in other kagome magnets[7,8,20,25,26], which show various atomic defects, there is no detectable defect over a large field of view. The experimental visualization of such a defect-free magnetic kagome lattice offers an unprecedented opportunity to explore its intrinsic topological quantum properties.

Next we measured the low-energy tunnelling spectrum of the manganese kagome lattice under an applied magnetic field (Fig. 2a, b). We find the zero-field spectra to be spatially homogeneous. When applying a 9-T magnetic field along the *c* axis, the spectra show drastic changes with the emergence of a series of states widely distributed in energy, which is a clear signature of Landau quantization. We find the Landau quantization of the kagome layer is unique within this material; as for the other observed lattice with stripe morphology, we do not detect a strong field response up to 9 T (Fig. 2c, d). This surface is likely to be the TbSn layer based on the aforementioned easy cleavage plane and the fact that R^{3+} surface ions may have dangling bonds favouring reconstruction[27]. Moreover, none of the reported tunnelling studies on kagome materials have shown Landau quantization[7,8,20,25,26]. Therefore, the Landau quantization of the magnetic manganese kagome lattice suggests that it is distinguishably in the quantum limit.

To understand the origin of this Landau quantization, we map its fan diagram in Fig. 3a by slowly increasing the magnetic field. Mapping out the Landau fan is a non-trivial task in tunnelling experiments, and there are only a few successful examples in quantum materials, including graphene[28], bismuth[29] and topological insulators[30,31]. In these cases, analysis of the Landau fan extracts precise band structure information in momentum space, but applying such methodology to a correlated topological magnet remains challenging. For a spin–orbit-coupled kagome lattice with out-of-plane magnetization, it is natural to consider the existence of spin-polarized Dirac fermions with a Chern gap[14,15]. We highlight several key features in the Landau fan diagram that constrain the analysis along this direction. First, the zero-field peak shifts almost linearly to lower energy with increasing field, which indicates the presence of magnetic polarization with a Zeeman term ($\Delta E = \frac{1}{2} g\mu_B B$, where *g* is the Landé *g*-factor and *B* is the magnetic field strength). The observation of a Zeeman shift rather than a splitting demonstrates that the electronic states are spin-polarized, which is crucial for the Chern-gap formation[14,15]. Second, below this state, the other Landau levels shift nonlinearly with a square-root-like field dependence, and their separation at 9 T decreases for levels at lower energies. Both these factors are consistent with Dirac-like fermions[28] featuring the energy spectrum $\varepsilon_n \approx \sqrt{|n|B}$ ($n = 0, \pm1, \pm2\ldots$ is the Landau level index number). Third, above the zero-field peak, an intense state emerges and shifts in parallel with it. These two states that shift linearly with the field are likely to define the expected Chern gap Δ that is determined by the intrinsic spin–orbit coupling. The zero-field peak may be formed by accumulated states from the top of the lower Dirac branch[7].

A Chern gap modifies the bare Dirac dispersion $\varepsilon_k = E_D \pm \hbar\mathbf{k}v$ into $E_k = E_D \pm \sqrt{(\Delta/2)^2 + (\hbar\mathbf{k}v)^2}$ (E_D is the Dirac cone energy, $\hbar$ is the reduced Planck constant, v is the Dirac velocity and $\mathbf{k}$ is the momentum vector). Hence to describe this Landau fan diagram, we start with a formula written as: $E_n = E_D \pm \sqrt{(\Delta/2)^2 + 2|n|e\hbar v^2 B} - \frac{1}{2} g\mu_B B$ (where *e* is the elementary charge). A simulation of the Landau fan data with this formula is shown in Fig. 3b with parameters $E_D = 130 \pm 4$ meV (where ± denotes the s.d. error), $\Delta = 34 \pm 2$ meV, $v = 4.2 \pm 0.3 \times 10^5$ m s^{-1} and $g = 52 \pm 2$. The large *g*-factor has also been reported in other topological materials, which

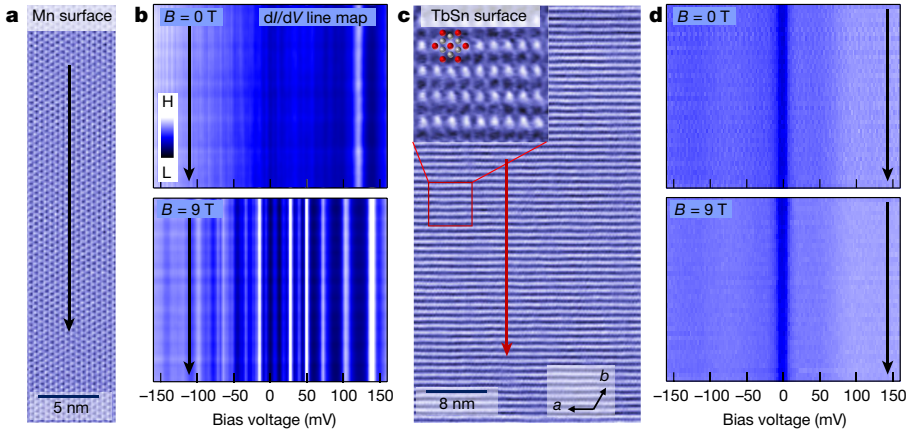

Fig. 2 | Distinct Landau quantization of the manganese kagome lattice. a, Topography of the manganese kagome lattice. **b**, The corresponding d*I*/d*V* line maps (along the black line in **a**) taken at $B = 0$ T (top) and $B = 9$ T (bottom). The 9-T data show intense modulation, which is associated with Landau quantization. **c**, Topography of the striped surface. Inset: magnified atomic view overlaid with a schematic TbSn lattice. **d**, Corresponding d*I*/d*V* line maps (along the red line in **c**) taken at $B = 0$ T (top) and $B = 9$ T (bottom). The arrows in **b** and **d** mark the line map direction.

may arise from the orbital contribution. In the kagome tight-binding model with nearest-neighbour hopping, the Dirac dispersions appear at the Brillouin zone corners. Our exploration of the band structure below the Fermi level via angle-resolved photoemission indeed finds linear dispersions near the zone corners with a similar Fermi velocity, which also reasonably connect to the Chern gapped Dirac band extracted from the tunnelling data, as shown in Fig. 3c. We further find that the gap extracted directly from the energy distance of the two peaks increases slightly with the field, correlating with that of the out-of-plane magnetization value M_C (Fig. 3d). The weak field dependence supports the interpretation that the Chern gap is not opened by the external field but induced by the intrinsic spin–orbit coupling[15]. The existence of predominant Chern gapped Dirac fermions just around the Fermi level is another key factor in driving this defect-free kagome lattice to the quantum limit.

The non-trivial topology of the Chern gap produces the dissipationless edge state. To visualize this bulk–boundary correspondence, we perform tunnelling measurements to map a step edge (Fig. 4a). Both the upper and lower layers of the step edge are surfaces formed by the manganese kagome lattices with a unit-cell step height of about 9 Å, and therefore have similar density of states. We observe a pronounced localized edge when mapping at energy within the Chern gap, while no clear edge state is detectable at other energies outside the gap, confirming the existence of the non-trivial in-gap edge state[32,33]. We also explore the tunnelling signal on the side cleaving surface (Fig. 4b). We perform mapping over a large area, and their direct Fourier transforms give rise to a quasiparticle scattering signal. We observe that quasiparticle scattering along the bulk edge direction is substantially reduced within the energy range of the Chern gap, in agreement with the dissipationless nature (lack of backscattering) of the Chern edge state. The magnetic Landau fan exhibiting a Chern gap and the emergence of in-gap edge states lack of backscattering together provide spectroscopic evidence for the topological bulk–boundary correspondence.

In addition to the bulk–boundary correspondence, Chern gapped Dirac fermions will also feature large Berry curvature[34–40]. This Berry curvature contribution to anomalous Hall conductivity is estimated[39] as $\sigma_{xy} = \frac{\Delta}{2E_D} \times e^2/h = (0.13 \pm 0.01)e^2/h$ based on the tunnelling data. Indeed, we observe the anomalous Hall signal ρ_{AH} in the Hall resistivity of the bulk crystal (Extended Data Fig. 3). When plotting ρ_{AH} against the square of the longitudinal resistivity ρ_{xx}^2, we observe a linear scaling (Fig. 4c), indicating a predominant intrinsic contribution[34–38]. From the linear fit ($\rho_{AH} = A + \sigma^{int}\rho_{xx}^2$, where A is a constant coefficient), we find that this intrinsic contribution is $\sigma^{int} = 121 \pm 6\ \Omega^{-1}\,cm^{-1}$. This amounts to $\sigma_{xy}^{int} = (0.14 \pm 0.01)e^2/h$ per manganese kagome layer, which agrees with the expected σ_{xy}, attesting to the Berry curvature correspondence of Chern gapped Dirac fermions.

Our observations of magnetic Landau quantization and bulk–boundary–Berry correspondence provide strong evidence in space and momentum for a quantum-limit Chern magnet. It is extremely rare to find a topological magnetic system featuring a quantized Landau fan, which requires defect-free magnetic material design and cutting-edge spectroscopy characterization. It is equally rare to find a large-Chern-gap system to demonstrate its topological correspondence, which is one of the key pursuits in the pertinent fundamental

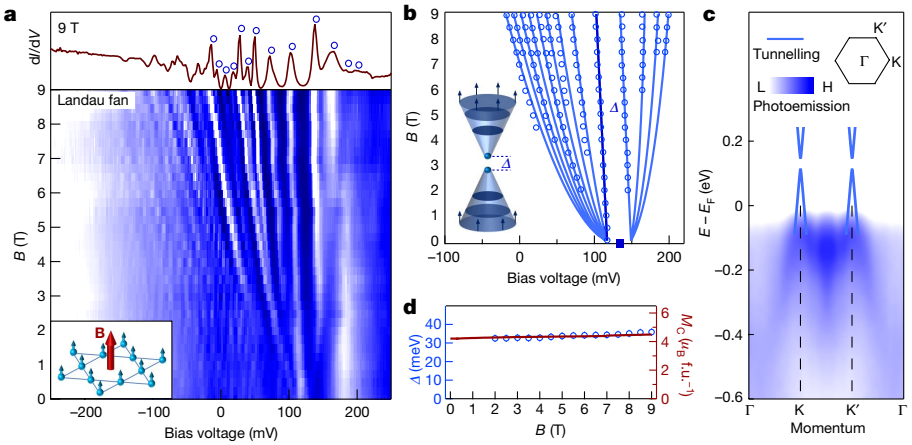

Fig. 3 | Quantum-limit visualization of Chern gapped Dirac fermions. **a**, Landau fan diagram of the kagome lattice. The inset illustrates the magnetic field applied perpendicular to the kagome lattice. The top panel shows the 9-T d*I*/d*V* spectrum, with Landau levels marked by open circles. **b**, Fitting the Landau fan data (open circles) with the spin-polarized and Chern gapped Dirac dispersion (solid lines). Inset: schematic of Landau quantization of Chern gapped Dirac fermions. **c**, Comparison of the dispersion obtained from tunnelling and photoemission. The inset shows the Brillouin zone for a kagome lattice. **d**, Dirac gap size (open circles) and out-of-plane magnetization (solid line) as a function of the magnetic field.

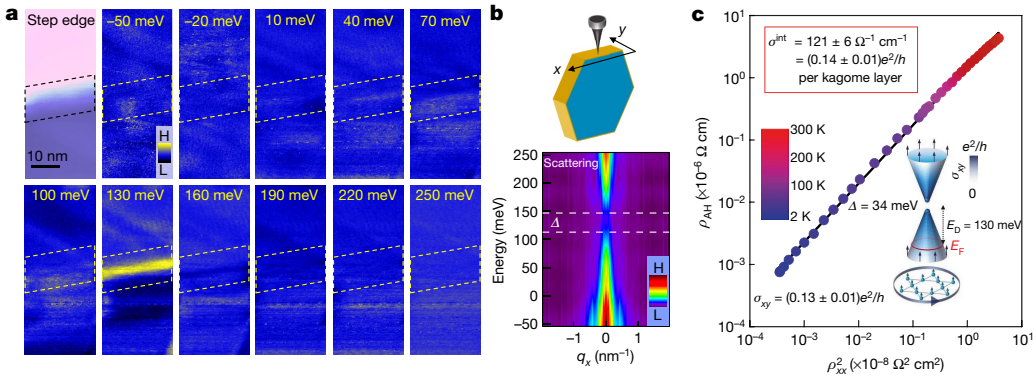

Fig. 4 | Correspondence of Chern gapped Dirac fermions with topological edge state and Berry curvature. a, dI/dV maps taken at different energies across a step edge (top left). The map taken within the Chern gap energy (130 meV) shows a pronounced step-edge state. **b**, Quasiparticle scattering along the bulk crystal edge direction (illustrated on top, q_x is the scattering vector along the edge direction). The dashed white lines in the scattering map mark the Chern gap energy determined by the Landau quantization. **c**, The anomalous Hall resistivity ρ_{AH} plotted against ρ_{xx}^2 in a logarithmic scale from 2 K to 300 K. The intrinsic Hall conductance is given by the slope of the line, which amounts to $(0.14 \pm 0.01)e^2/h$ per manganese kagome layer (top inset). The bottom inset illustrates the Berry curvature contribution to the Hall conductivity from Chern gapped Dirac fermions, which is $(0.13 \pm 0.01)e^2/h$ per manganese kagome layer based on the tunnelling data.

research area of topological matter[9,10]. Given that there are dozens of compounds with similar structures to $TbMn_6Sn_6$ that host kagome lattices with a variety of magnetic structures and wide tunability of the lattice constant, our findings provide a valuable guideline for discovering other intimately related, yet hitherto unknown, topological or quantum phenomena.

Online content

Any methods, additional references, Nature Research reporting summaries, source data, extended data, supplementary information, acknowledgements, peer review information; details of author contributions and competing interests; and statements of data and code availability are available at https://doi.org/10.1038/s41586-020-2482-7.

1. Keimer, B. & Moore, J. E. The physics of quantum materials. *Nat. Phys.* **13**, 1045–1055 (2017).
2. Sachdev, S. Topological order, emergent gauge fields, and Fermi surface reconstruction. *Rep. Prog. Phys.* **82**, 014001 (2019).
3. Hasan, M. Z. et al. Topological insulators, topological superconductors and Weyl fermion semimetals: discoveries, perspectives and outlooks. *Phys. Scr.* **2015**, 014001 (2015); corrigendum **2016**, 019501 (2016).
4. He, K., Wang, Y. & Xue, Q.-K. Topological materials: quantum anomalous Hall system. *Annu. Rev. Condens. Matter Phys.* **9**, 329–344 (2018).
5. Franz, M. & Rozali, M. Mimicking black hole event horizons in atomic and solid-state systems. *Nat. Rev. Mater.* **3**, 491–501 (2018).
6. Armitage, N. P., Mele, E. J. & Vishwanath, A. Weyl and Dirac semimetals in three-dimensional solids. *Rev. Mod. Phys.* **90**, 015001 (2018).
7. Yin, J. X. et al. Giant and anisotropic many-body spin–orbit tunability in a strongly correlated kagome magnet. *Nature* **562**, 91–95 (2018).
8. Yin, J.-X. et al. Negative flat band magnetism in a spin–orbit-coupled correlated kagome magnet. *Nat. Phys.* **15**, 443–448 (2019).
9. Thouless, D. J. et al. Quantized Hall conductance in a two-dimensional periodic potential. *Phys. Rev. Lett.* **49**, 405–408 (1982).
10. Haldane, F. D. M. Model for a quantum Hall effect without Landau levels: condensed-matter realization of the "parity anomaly". *Phys. Rev. Lett.* **61**, 2015–2018 (1988).
11. Chang, C. Z. et al. Experimental observation of the quantum anomalous Hall effect in a magnetic topological insulator. *Science* **340**, 167–170 (2013).
12. Sharpe, A. L. et al. Emergent ferromagnetism near three-quarters filling in twisted bilayer graphene. *Science* **365**, 605–608 (2019).
13. Zou, J., He, Z. & Xu, G. The study of magnetic topological semimetals by first principles calculations. *npj Comput. Mater.* **5**, 96 (2019).
14. Tang, E., Mei, J. W. & Wen, X. G. High-temperature fractional quantum Hall states. *Phys. Rev. Lett.* **106**, 236802 (2011).
15. Xu, G., Lian, B. & Zhang, S.-C. Intrinsic quantum anomalous Hall effect in the kagome lattice $Cs_2LiMn_3F_{12}$. *Phys. Rev. Lett.* **115**, 186802 (2015).
16. Nakatsuji, S., Kiyohara, N. & Higo, T. Large anomalous Hall effect in a non-collinear antiferromagnet at room temperature. *Nature* **527**, 212–215 (2015).
17. Ye, L. et al. Massive Dirac fermions in a ferromagnetic kagome metal. *Nature* **555**, 638–642 (2018).
18. Liu, E. et al. Giant anomalous Hall effect in a ferromagnetic kagome-lattice semimetal. *Nat. Phys.* **14**, 1125–1131 (2018).
19. Kang, M. et al. Dirac fermions and flat bands in the ideal kagome metal FeSn. *Nat. Mater.* **19**, 163–169 (2020).
20. Lin, Z. et al. Flatbands and emergent ferromagnetic ordering in Fe_3Sn_2 kagome lattices. *Phys. Rev. Lett.* **121**, 096401 (2018).
21. Kane, C. L. & Mele, E. J. Quantum spin Hall effect in graphene. *Phys. Rev. Lett.* **95**, 226801 (2005).
22. Venturini, G., Elldrissi, B. C. & Malaman, B. Magnetic properties of RMn_6Sn_6 (R = Sc, Y, Gd–Tm, Lu) compounds with $HfFe_6Ge_6$ type structure. *J. Magn. Magn. Mater.* **94**, 35–42 (1991).
23. Malaman, B. et al. Magnetic properties of RMn_6Sn_6 (R = Gd–Er) compounds from neutron diffraction and Mössbauer measurements. *J. Magn. Magn. Mater.* **202**, 519–534 (1999).
24. El Idrissi, B. C., Venturini, G., Malaman, B. & Fruchart, D. Magnetic structures of $TbMn_6Sn_6$ and $HoMn_6Sn_6$ compounds from neutron diffraction study. *J. Less Common Met.* **175**, 143–154 (1991).
25. Jiao, L. et al. Signatures for half-metallicity and nontrivial surface states in the kagome lattice Weyl semimetal $Co_3Sn_2S_2$. *Phys. Rev. B* **99**, 245158 (2019).
26. Yang, H.-H. et al. Scanning tunneling microscopy on cleaved $Mn_3Sn(0001)$ surface. *Sci. Rep.* **9**, 9677 (2019).
27. Rößler, S. et al. Hybridization gap and Fano resonance in SmB_6. *Proc. Natl Acad. Sci. USA* **111**, 4798–4802 (2014).
28. Miller, D. L. et al. Observing the quantization of zero mass carriers in graphene. *Science* **324**, 924–927 (2009).
29. Feldman, B. E. et al. Observation of a nematic quantum Hall liquid on the surface of bismuth. *Science* **354**, 316–321 (2016).
30. Okada, Y., Serbyn, M., Lin, H. & Walkup, D. Observation of Dirac node formation and mass acquisition in a topological crystalline insulator. *Science* **341**, 1496–1499 (2013).
31. Hanaguri, T., Igarashi, K. & Kawamura, M. Momentum-resolved Landau-level spectroscopy of Dirac surface state in Bi_2Se_3. *Phys. Rev. B* **82**, 081305 (2010).
32. Wu, R. et al. Evidence for topological edge states in a large energy gap near the step edges on the surface of $ZrTe_5$. *Phys. Rev. X* **6**, 021017 (2016).
33. Tang, S. et al. Quantum spin Hall state in monolayer 1T′-WTe_2. *Nat. Phys.* **13**, 683–687 (2017).
34. Tian, Y. et al. Proper scaling of the anomalous Hall effect. *Phys. Rev. Lett.* **103**, 087206 (2009).
35. Nagaosa, N., Sinova, J., Onoda, S., MacDonald, A. H. & Ong, N. P. Anomalous Hall effect. *Rev. Mod. Phys.* **82**, 1539–1592 (2010).
36. Haldane, F. D. M. Berry curvature on the Fermi surface: anomalous Hall effect as a topological Fermi-liquid property. *Phys. Rev. Lett.* **93**, 206602 (2004).
37. Yates, J. et al. Spectral and Fermi surface properties from Wannier interpolation. *Phys. Rev. B* **75**, 195121 (2007).
38. Chang, M.-C. et al. Berry phase, hyperorbits, and the Hofstadter spectrum: semiclassical dynamics in magnetic Bloch bands. *Phys. Rev. B* **53**, 7010–7023 (1996).
39. Sinitsyn, N. A., MacDonald, A. H., Jungwirth, T., Dugaev, V. K. & Sinova, J. Anomalous Hall effect in a two-dimensional Dirac band: the link between the Kubo–Streda formula and the semiclassical Boltzmann equation approach. *Phys. Rev. B* **75**, 045315 (2007).
40. Kou, X. et al. Scale-invariant quantum anomalous Hall effect in magnetic topological insulators beyond the two-dimensional limit. *Phys. Rev. Lett.* **113**, 137201 (2014).

Methods

Single-crystal growth

Single crystals of $TbMn_6Sn_6$ were prepared by using the flux growth method with tin as the flux[41,42]. A mixture of $(TbMn_6)_{4.5}Sn_{95.5}$ elements was packed into an alumina crucible, which was then sealed with a piece of quartz wool as 'catch filter' in a quartz ampoule under vacuum. The ampoule was heated to 1,000 °C and slowly cooled to the spin temperature of 600 °C over several days. After centrifugation, several hexagonal, flat, millimetre-sized crystals with metallic luster were found in the crucible. The temperature-dependent resistivity of the crystals shows a metal-like profile with a residue resistivity ratio larger than 100, indicating the high quality of the crystals.

Scanning tunnelling microscopy characterization

Single crystals with size up to 4 mm × 4 mm × 1 mm were cleaved mechanically in situ at 77 K in ultrahigh vacuum conditions, and then immediately inserted into the microscope head, already at ^{4}He base temperature (4.2 K). The magnetic field was applied with zero-field cooling. To acquire the field-dependent tunnelling data, we first withdrew the tip about 1 μm from the sample. We then slowly increased the field by 0.5 T, and then set the superconducting magnet into the persistent mode. We then approached the tip to the same surface and scanned the image to locate the same atomic position. After allowing for an additional 1 h of relaxation time of the system, we performed high-resolution spectroscopy at this field. We repeated this procedure for the field from 0 T to 9 T. We also checked the tunnelling spectroscopy at −1 T, −2 T and −3 T, confirming the consistency of the Landau fan data with reverse magnetization. Tunnelling conductance spectra were obtained with an iridium/platinum tip using standard lock-in amplifier techniques with a root-mean-square oscillation voltage of 1 meV and a lock-in frequency of 877 Hz. Topographic images were taken with a tunnelling junction setup of voltage $V = -100$ mV and current $I = 0.05–0.5$ nA. The conductance maps were taken with a tunnelling junction setup of $V = -250$ mV and $I = 1$ nA.

Transmission electron microscopy characterization

Thin lamellae were prepared by focused ion beam cutting. All samples for experiments were polished using a 2-kV gallium ion beam to minimize the surface damage caused by the high-energy ion beam. Transmission electron microscopy imaging, atomic-resolution high-angle annular dark-field scanning transmission electron microscopy imaging and atomic-level energy-dispersive X-ray spectroscopy mapping were performed on a Titan Cubed Themis 300 double Cs-corrected scanning/transmission electron microscope equipped with an extreme field emission gun source operated at 300 kV with a super-X energy-dispersive spectrometry system.

Electrical transport and magnetization measurements

Both longitudinal and Hall resistivities were measured in a commercial physical property measurement system (PPMS, Quantum Design) by using a standard four-probe method. An a.c. resistance bridge (Model 372, Lakeshore) was used to measure the small signals at low temperatures ($T < 100$ K). Field-antisymmetrization was used for Hall measurement to subtract the longitudinal resistivity component. Magnetization measurements were performed in a commercial superconducting quantum interference device (Quantum Design) with the field applied along the c axis. We used the reading microscope to measure the size of the sample, and the typical sample thickness for our transport measurement is 0.1 mm. The main source of the Hall resistivity error comes from the thickness of the sample d, which is around 5%. We used the thickness to calculate the Hall resistivity, $\rho_{yx} = R_{yx} \times d$. For $TbMn_6Sn_6$, the one-unit cell contains two manganese kagome layers, so we divide e^2/h by $c/2$ (half of the unit cell constant along the c axis) to obtain the quantum-limit value of anomalous Hall conductance.

Extended crystal structure characterization

$TbMn_6Sn_6$ has a layered crystal structure with the space group $P6/mmm$ (number 191) and lattice constants $a = 5.53$ Å and $c = 9.023$ Å (ref. [24]). It is formed by stacking of $TbSn_2$–Mn_3–Sn–Sn_2–Sn–Mn_3–$TbSn_2$ as shown in Extended Data Fig. 1. In the $TbSn_2$ layer, the Sn_2 forms a hexagonal lattice with the terbium atoms at the centre of the hexagons. Each Sn_2 layer is sandwiched by $TbSn_2$ layers and tin atoms form hexagonal structures sitting directly below (above) the tin atoms of the $TbSn_2$ layer. The Mn_3–Sn layers are located between the $TbSn_2$ and Sn_2 layers. In each Mn_3–Sn layer, the manganese atoms form a kagome lattice and tin atoms are positioned at the centre of each kagome pattern, with tin atoms being located far below (above) the manganese layers. Hence it can be viewed as a pure manganese layer of kagome structure. This pure kagome layer is distinguished from the kagome lattice containing additional tin atoms in other well-known kagome magnets, including Fe_3Sn_2, FeSn, $Co_3Sn_2S_2$ and Mn_3Sn.

The single-crystal image is shown in Extended Data Fig. 2a. The crystal has a flake-like hexagonal shape and is easily cleaved to yield a shining surface, both of which are consistent with its quasi-two-dimensional structure. The Laue diffraction pattern of the bulk crystal shows sharp Bragg spots with hexagonal symmetry in Extended Data Fig. 2b, supporting high-quality crystallization. The in-plane, atomic-resolution, cross-sectional image and its elemental analysis taken by a scanning transmission electron microscope are provided in Extended Data Fig. 2c–e, demonstrating the atomic arrangement consistent with its crystal structure.

Extended magnetization and electrical transport data

$TbMn_6Sn_6$ manifests a spin reorientation transition at about 310 K. Below this temperature, the easy-magnetization direction changes from the basal plane to the c axis[23,24,42,43]. Extended Data Fig. 3a shows that the single-crystalline $TbMn_6Sn_6$ is a hard magnet with considerable hysteresis below 200 K. The coercive field is about 1 T below 100 K, much larger than that for other kagome magnets.

We systematically explore its anomalous Hall resistivity under the magnetic field at different temperatures (Extended Data Fig. 3b). The Hall resistivity shows sharp steps/loops from 300 K to 2 K, indicating the anomalous Hall contribution ρ_{AH}. The top inset in Extended Data Fig. 3b shows the temperature evolution of the longitudinal resistivity ρ_{xx} and anomalous Hall resistivity ρ_{AH}.

Extended quantum oscillation data

We collect transport data on the single crystals under a magnetic field up to 14 T in Extended Data Fig. 4a. Above 7 T, quantum oscillations could be identified in the magnetoresistance after subtracting a smooth background, revealing the Landau quantization from the bulk crystal. These oscillations damp slowly with temperature and are observable at 20 K. Fast Fourier transformation (FFT) analysis reveals a dominant frequency of 96 T. According to the Onsager relation[44], $A_k = \frac{2\pi e}{\hbar}F$, where A_k is the extremal cross-sectional area of the Fermi surface and F is the measured frequency, this corresponds to a Fermi length k_F of 0.054 Å^{-1}, if the extremal cross-sectional area is assumed to be circular ($A_k = \pi k_F^2$). This matches the k_F (0.05 ± 0.01 Å^{-1}) of the Dirac band from angle-resolved photoemission, which is consistent with the tunnelling data as well (Fig. 3c). Fitting the temperature evolution of FFT signal to the standard Lifshitz–Kosevich formula[44], $\Delta\rho(T) \propto \frac{2\pi^2 k_B T m^*/(eB\hbar)}{\sinh[2\pi^2 k_B T m^*/(eB\hbar)]}$, with k_B being the Boltzmann constant and m^* the cyclotron mass, we estimate the cyclotron mass of the hole carriers to be $(0.13 \pm 0.01)m_e$, where m_e is the free electron mass. This agrees with the cyclotron mass of the Dirac electrons based on the tunnelling data $E_D/v^2 = (0.13 \pm 0.01)m_e$.

We further trace the angle dependence of the Fermi morphology by varying field direction in transport measurements. As shown in Extended Data Fig. 4c, the FFT frequency changes in a $1/\cos\theta$ manner,

where θ is the tilted angle from the crystallographic c axis, which indicates that this Fermi surface in the bulk crystal is two-dimensional-like. This is consistent with the tunnelling data that the Landau quantization of Dirac electrons is localized on the manganese kagome lattice. Therefore, the transport spectroscopic consistency in the Fermi length, cyclotron mass and quasi-two-dimensional nature of the Landau quantization signal support the bulk quasi-two-dimensional nature of the Dirac electrons in this kagome magnet.

We also note that in Extended Data Fig. 4b, in addition to the main peak, there are additional bumps in the FFT signal of the quantum oscillation data. This is echoed in the tunnelling Landau quantization data showing additional bumps that exist near the Fermi energy, which are much weaker than the main Dirac Landau levels. These second-order signals could be related to additional Fermi surfaces contributions in this system.

Extended anomalous Hall transport data

The spectroscopic data suggest that the Chern gap is just above the Fermi level. Proper electron doping or gating could drive the Fermi level into the Chern gap to enhance the Hall response. Here we explore the possibility of iron doping. The $Tb(Mn_{1-x}Fe_x)_6Sn_6$ compounds ($x = 0.1$, 0.2) were prepared using the same method used for $TbMn_6Sn_6$. We observe that with iron doping, the intrinsic Hall conductance increases substantially and is close to the quantum limit at $x = 0.1$, while it drops on further doping (at $x = 0.2$) as shown in Extended Data Fig. 5. This electron-doping exploration is consistent with the existence of a Chern gap above the Fermi level.

Extended tunnelling data

Inspired by the step-edge-state observation (Fig. 4a), we explore the tunnelling signal on the side cleaving surface (Extended Data Fig. 6a). Tunnelling on the side surface is challenging as there is no natural cleaving plane, and the tunnelling signal can often be unstable. We first obtain stable tunnelling on a large area of the side surface (Extended Data Fig. 6b) through extensive exploration. Then, we perform dI/dV mapping over an area of 60 × 60 nm, and their direct Fourier transforms give rise to the quasiparticle scattering signals. We find that the quasiparticle scattering along the bulk edge direction is substantially reduced within the energy range of the Chern gap determined by the Landau quantization (Extended Data Fig. 6c), indicating the absence of backscattering signal of the in-gap edge states. This scattering observation supports the dissipationless nature of the edge state within the Chern gap.

Extended angle-resolved photoemission data

Photoemission measurements were conducted at a synchrotron beamline. Single crystals were cleaved in situ in ultrahigh vacuum conditions at a temperature of 12 K on the photoemission manipulator and then transferred to measurement position while maintaining temperature and pressure. Photoemission measurements were conducted using 90–120-eV incident photons with linear horizontal polarization, such that the light was s-polarized with respect to the sample surface. A Scienta R4000 analyser was used to collect angle-resolved photoemission spectra with an energy resolution of 30 meV and angular resolution of 0.2°. Extended Data Fig. 7 shows additional photoemission data for this material.

The fundamental model for a kagome Chern magnet

The effective Hamiltonian for a ferromagnetic kagome lattice (Extended Data Fig. 8a) can be written as

$$H = H_k + H_{SOI} + H_m$$

where H_k describes the spinless tight-binding model of the kagome lattice with nearest-neighbour hopping t and lattice spacing a

$$H_k = -\sum_{\langle ij\rangle} t c_i^+ c_j - \mu \sum_i c_i^+ c_i$$

Here $c_j(c_i^+)$ is the electron annihilation (creation) operator at site j (or site i) in the spinor notation. μ is the chemical potential.

H_{SOI} is the Kane–Mele type spin–orbit interaction

$$H_{SOI} = i \sum_{ij} \lambda v_{ij} (c_i^+ s_z c_j)$$

where λ is the interaction amplitude, s_z is the spin Pauli matrix and $v_{ij} = 2/\sqrt{3}(\mathbf{d}_i \times \mathbf{d}_j) \cdot \mathbf{z}$ with $\mathbf{d}_i$ and $\mathbf{d}_j$ denoting the unit vectors along the two bonds that the electron traverses from the site i to site j on the kagome lattice.

H_m is the double exchange coupling J_H between the ferromagnetic moment $\mathbf{m}_i$ and the conduction electrons:

$$H_m = -J_H \sum_i c_i^+ \mathbf{s} \cdot \mathbf{m}_i c_i$$

Since $TbMn_6Sn_6$ is ferrimagnetically ordered in the z direction, we can use a spinless model to describe this effective model with

$$H_{eff} = -\sum_{\langle ij\rangle} t f_i^+ f_j + i \sum_{ij} \lambda v_{ij} (f_i^+ f_j) + (E_D + t) \sum_i f_i^+ f_i$$

where f_i is the fermion operator in the low-energy spin z component and E_D is the Dirac cone energy. Expanding around $K_\pm = \left(\pm\frac{2\pi}{3a}, 0\right)$ (Extended Data Fig. 8b), a Chern gapped Dirac model can be obtained as

$$H_D = \hbar v (k_x \sigma_y - k_y \sigma_x) + \frac{\Delta}{2}\sigma_z + E_D$$

where σ_i ($i = x, y, z$) are the Pauli matrices of pseudospin, v is the Dirac velocity and Δ is the gap at the Dirac point (Extended Data Fig. 8c, d). In the above tight-binding model, $v = \sqrt{3}t$ and $\Delta = 2\sqrt{3}\lambda$.

Next, we carry out an open boundary strip calculation. As shown in Extended Data Fig. 8e, there is a clear chiral edge dispersion when $\lambda = 0.1t$ and $E_D = 0$ in accordance with bulk Chern number $C = 1$. Using the Kubo formalism[40], the Hall conductivity σ_{xy} can be calculated to be:

$$\sigma_{xy} = \frac{e^2}{h} \frac{\Delta/2}{\sqrt{(\Delta/2)^2 + (\hbar v k_F)^2}} = \frac{e^2}{h} \frac{\Delta}{2E_D}$$

where the k_F is the Fermi length, as shown in Extended Data Fig. 8f. From the above equation, σ_{xy} is quantized to e^2/h when the chemical potential is within the Chern gap, in which case we set $k_F = 0$.

In addition, similar to graphene and if the chemical potential is well outside the Chern gap, the cyclotron mass can be obtained[45] as

$$m^* = \frac{1}{2\pi}\left[\frac{\partial A(E)}{\partial E}\right]_{E=E_F} = \frac{E_D}{v^2}$$

where $A(E)$ is the area in k space enclosed by the orbit, and E_F is the Fermi energy.

Considering the Landau level of the Chern gapped Dirac model, we can apply a uniform magnetic field B and choose the Landau gauge: $A = B(-y, 0, 0)$. The effective Hamiltonian becomes

$$H_D = v[(\hat{p}_x - eBy)\sigma_y - \hat{p}_y \sigma_x] + \frac{\Delta}{2}\sigma_z + E_D - \frac{g\mu_B}{2}B$$

where $\hat{p}_x$ (or $\hat{p}_y$) is the momentum operator in the x (or y) direction.

As k_x is still a good quantum number, one can diagonalize the Hamiltonian in the y harmonic oscillator basis[45]. The Landau level eigenvalues are given by

$$E_n = E_D \pm \sqrt{(\Delta/2)^2 + 2|n|e\hbar v^2 B} - \frac{1}{2} g\mu_B B (n = 0, \pm 1, \pm 2 \ldots)$$

First-principles calculation

The electronic band structures of $TbMn_6Sn_6$ were computed using the projector augmented wave method as implemented in the Vienna ab initio simulation package[46–48] version 5.4.4 within the generalized gradient approximation[49] scheme. The spin–orbit coupling was included self-consistently in the calculations of electronic structures with a k-point mesh of 13 × 13 × 7. The experimental lattice structure parameters and magnetic structure were used. We used Tb d orbitals, Mn s and d orbitals, and Sn p orbitals to construct Wannier functions, without performing the procedure for maximizing localization. The simulated scanning tunnelling microscope image was based on the calculation of the real-space charge density distribution according to the Tersoff–Hamann approach, which was acquired by the program HIVE[50].

The calculated bulk band structure along the high-symmetry directions is shown in Extended Data Fig. 9a (with spin–orbit coupling) and Extended Data Fig. 9b (without spin–orbit coupling), where we find a magnetic Dirac cone structure at the Brillouin zone corners (K and K′), consistent with the angle-resolved photoemission exploration. The bands around −0.2 eV are relatively flat in contrast with the steep Dirac bands, which can be the flat band candidate. For the manganese-terminating surface, the simulated topographic image in Extended Data Fig. 9c shows the kagome symmetry consistent with experimental data. We further find that 90% of the spectral weight of the Dirac bands is from the manganese in-plane 3d orbitals including d_{xy} and $d_{x^2-y^2}$ (Extended Data Fig. 9d), which is consistent with their quasi-two-dimensional nature in the experiment. Moreover, the Dirac band features a high Fermi velocity of 4×10^5 m s^{-1}, and a large energy gap of 35 meV, both of which are consistent with the Dirac band dispersion extracted from the tunnelling data on the manganese kagome layer on the energy scale (blue curve in Extended Data Fig. 9d). The magnetic Dirac gap is opened by atomic spin–orbit coupling, as shown in Extended Data Fig. 9d, e, as well as in Extended Data Fig. 9a, b, consistent with the fundamental kagome model.

Features of a quantum-limit Chern magnet in real and momentum space

Extended Data Fig. 10a, b illustrates our key findings in this quantum-limit Chern magnet. In momentum space, spin-polarized Dirac fermions with a Chern gap exhibit Landau quantization. In real space, spin–orbit-coupled magnetic kagome lattice carries a topological edge state within the Chern energy gap.

Data availability

The data that support the findings of this study are available from the corresponding authors upon reasonable request. Source data are provided with this paper.

41. Canfield, P. C. & Fisk, Z. Growth of single crystals from metallic fluxes. *Phil. Mag. B* **65**, 1117–1123 (1992).
42. Clatterbuck, D. M. & Gschneidner, K. A. Magnetic properties of RMn_6Sn_6 (R = Tb, Ho, Er, Tm, Lu) single crystals. *J. Magn. Magn. Mater.* **207**, 78–94 (1999).
43. Zajkov, N. K. et al. Magnetization processes in the $TbMn_6Sn_6$ compound. *J. Alloys Compd* **309**, 26–30 (2000).
44. Shoenberg, D. *Magnetic Oscillations in Metals* (Cambridge Univ. Press, 2009).
45. Castro Neto, A. H., Guinea, F., Peres, N. M. R., Novoselov, K. S. & Geim, A. K. The electronic properties of graphene. *Rev. Mod. Phys.* **81**, 109–162 (2009).
46. Blöchl, P. E. Projector augmented-wave method. *Phys. Rev. B* **50**, 17953–17979 (1994).
47. Kresse, G. & Joubert, D. From ultrasoft pseudopotentials to the projector augmented-wave method. *Phys. Rev. B* **59**, 1758–1775 (1999).
48. Kresse, G. & Furthmüller, J. Efficiency of ab-initio total energy calculations for metals and semiconductors using a plane-wave basis set. *Comput. Mater. Sci.* **6**, 15–50 (1996).
49. Perdew, J. P., Burke, K. & Ernzerhof, M. Generalized gradient approximation made simple. *Phys. Rev. Lett.* **77**, 3865–3868 (1996).
50. Vanpoucke, D. E. P. & Brocks, G. Formation of Pt-induced Ge atomic nanowires on Pt/Ge(001): a density functional theory study. *Phys. Rev. B* **77**, 241308 (2008).

Acknowledgements We thank B. Sales and Y. Xiong for providing other kagome materials for comparison study. We thank P. W. Anderson, D. Huse, D. Haldane, S. Wu and N. P. Ong for discussions. Experimental and theoretical work at Princeton University was supported by the Gordon and Betty Moore Foundation (GBMF4547; M.Z.H.). The material characterization (ARPES) is supported by the United States Department of Energy (US DOE) under the Basic Energy Sciences programme (grant number DOE/BES DE-FG-02-05ER46200). The work in Peking University was supported by the National Natural Science Foundation of China numbers U1832214 and 11774007, the National Key R&D Program of China (2018YFA0305601) and the strategic Priority Research Program of Chinese Academy of Sciences (XDB28000000). Work at Princeton's Imaging and Analysis Center is partially supported by the Princeton Center for Complex Materials, a National Science Foundation (NSF)-MRSEC program (DMR-1420541). Work at Boston College was supported by the US Department of Energy, Basic Energy Sciences grant number DE-FG02-99ER45747. T.N. acknowledges supports from the European Union's Horizon 2020 research and innovation programme (ERC-StG-Neupert-757867-PARATOP). T.A.C. acknowledges support by the National Science Foundation Graduate Research Fellowship Program under grant number DGE-1656466. This research used resources of the Advanced Light Source, a DOE Office of Science User Facility under contract number DE-AC02-05CH11231. We thank S.-K. Mo for support at beamline 10.0.1 of the Advanced Light Source. We acknowledge Diamond Light Source for time on beamline i05 under Proposal SI22332-1. We thank C. Cacho and T. Kim for support at beamline i05 of Diamond Light Source. T.-R.C. was supported by the Young Scholar Fellowship Program from the Ministry of Science and Technology (MOST) in Taiwan, under a MOST grant for the Columbus Program MOST109-2636-M-006-002, National Cheng Kung University, Taiwan, and National Center for Theoretical Sciences, Taiwan. This work was supported partially by the MOST, Taiwan, grant MOST107-2627-E-006-001. This research was supported in part by Higher Education Sprout Project, Ministry of Education to the Headquarters of University Advancement at National Cheng Kung University (NCKU). M.Z.H. acknowledges support from Lawrence Berkeley National Laboratory and the Miller Institute of Basic Research in Science at the University of California, Berkeley in the form of a Visiting Miller Professorship.

Author contributions J.-X.Y., S.S.Z. and N.S. conducted the scanning tunnelling microscopy experiments in consultation with M.Z.H.; W.M., X.X. and H.Z. synthesized and characterized the magneto-transport of samples in consultation with S.J.; G. Cheng and N.Y. conducted the transmission electron microscopy experiments; T.A.C. and X.P.Y. conducted the angle-resolved photoemission experiments; H.-J.T., K.J., B.L., Z.S., G. Chang, T.-R.C., H.L., T.N. and Z.W. carried out the theoretical analysis in consultation with J.-X.Y., S.J. and M.Z.H.; I.B., D.M., M.L., Z.-J.C., B.S. and H.Z. contributed to the calibration of the measurement; J.-X.Y., W.M., S.J. and M.Z.H performed the data analysis and figure development and wrote the paper with contributions from all authors; M.Z.H. supervised the project. All authors discussed the results, interpretation and conclusion.

Competing interests The authors declare no competing interests.

Additional information
Correspondence and requests for materials should be addressed to J.-X.Y., S.J. or M.Z.H.

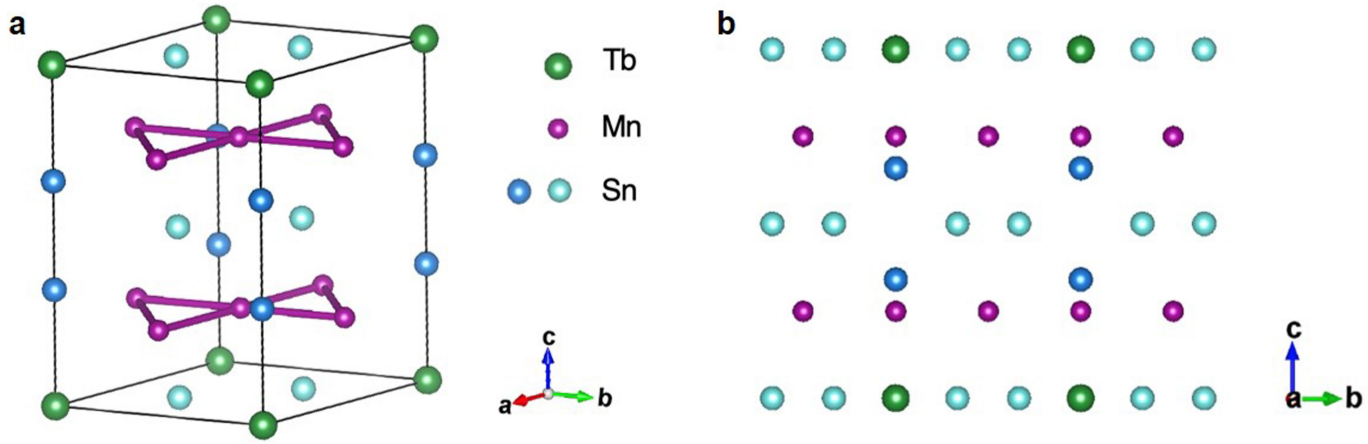

Extended Data Fig. 1 | Crystal structure of $TbMn_6Sn_6$. a, Crystal structure of $TbMn_6Sn_6$. **b**, Side view of the crystal structure.

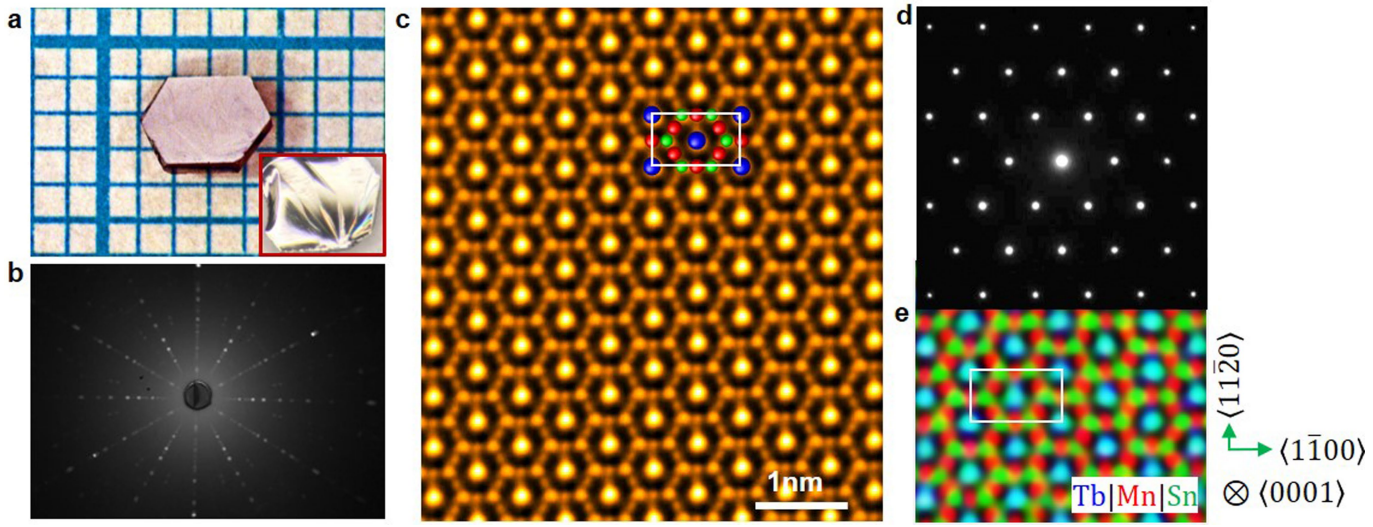

Extended Data Fig. 2 | Crystal structure characterization. a, Single-crystal image of $TbMn_6Sn_6$. The inset is an image of a cleaved crystal. **b**, Laue diffraction image of $TbMn_6Sn_6$. **c**, In-plane atomic-resolution image of $TbMn_6Sn_6$ taken by a scanning transmission electron microscope, showing the in-plane lattice arrangement. **d**, In-plane electron diffraction pattern of the crystal taken by transmission electron microscopy, showing hexagonal symmetry. **e**, In-plane elemental mapping by an energy dispersive X-ray detector. All data were taken at 300 K.

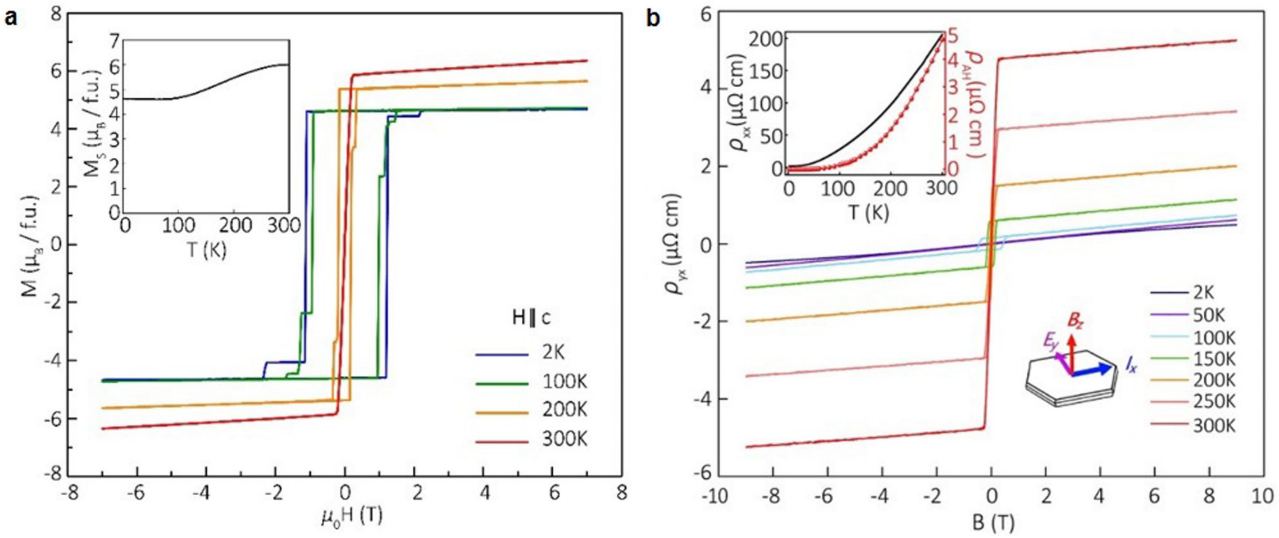

Extended Data Fig. 3 | Magnetization and transport data. a, Magnetic hysteresis loop with field applied along the *c* axis at different temperatures. Inset: the saturated magnetic moment at 0 T versus temperature. **b**, Hall resistivity measured as a function of the magnetic field at different temperatures. The bottom inset illustrates the geometry of the measurement, where the field is applied along the *c* axis and current is applied along the *a* axis of the crystal. Top inset: temperature evolution of the longitudinal resistivity ρ_{xx} and anomalous Hall resistivity ρ_{AH}.

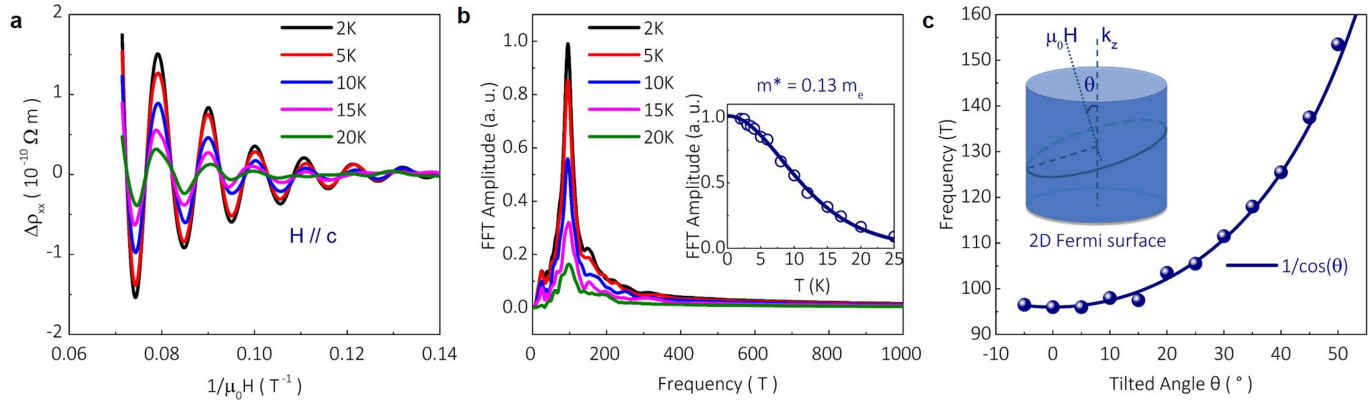

Extended Data Fig. 4 | Quantum oscillation data. a, Oscillatory component of magnetoresistance at different temperatures after subtracting a smooth background. **b**, FFT spectrum of quantum oscillations in **a**, showing a principle frequency of 96 T. Inset: fitting of the temperature evolution of this peak amplitude with the Lifshitz–Kosevich formula, yielding a cyclotron mass of $0.13 \pm 0.01\, m_e$. **c**, Angle dependence of the oscillatory frequency. The magnetic field is tilted from the crystallographic *c* axis to the *a* axis. The solid line is a fit to the function $1/\cos\theta$. Inset: a sketch of a two-dimensional Fermi surface, whose cross-sectional area evolves in a $1/\cos\theta$ manner when field direction is tilted θ away from the central axis.

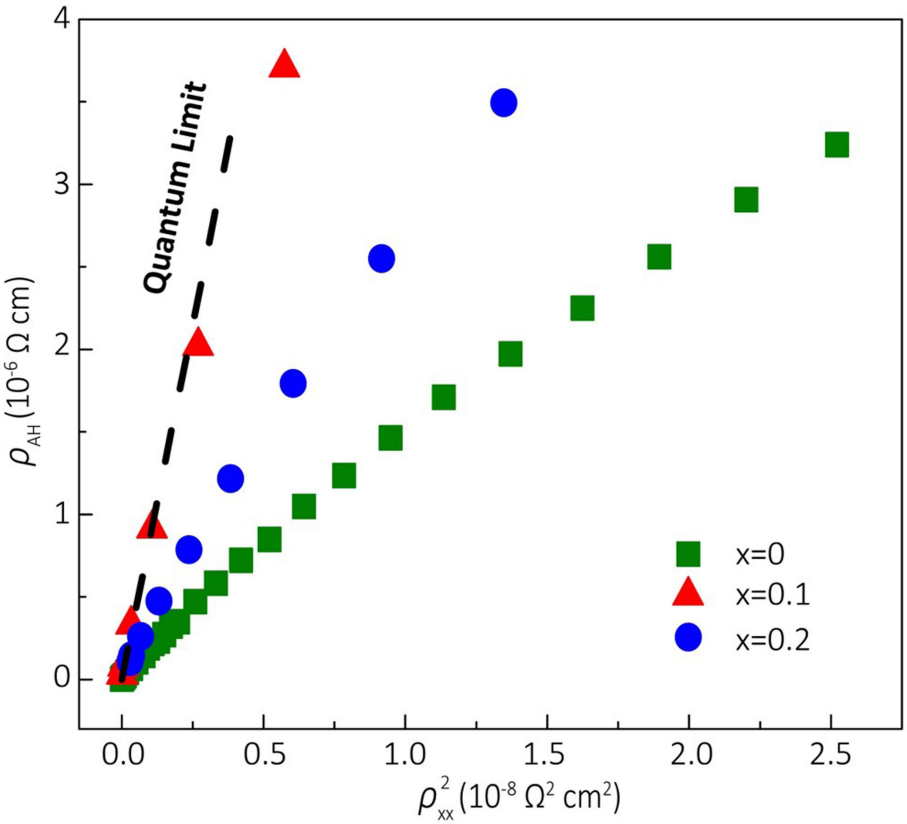

Extended Data Fig. 5 | Anomalous Hall transport data. The anomalous Hall resistivity ρ_{AH} plotted against ρ_{xx}^2 from 2 K to 300 K in $Tb(Mn_{1-x}Fe_x)_6Sn_6$ (Fe-doped $TbMn_6Sn_6$). The near-linear scaling indicates an intrinsic Berry curvature contribution to the anomalous Hall effect as the slope of each data set, which has a non-monotonic variation with doping. The black dotted line is the quantum-limit Hall value assuming one e^2/h per manganese kagome layer.

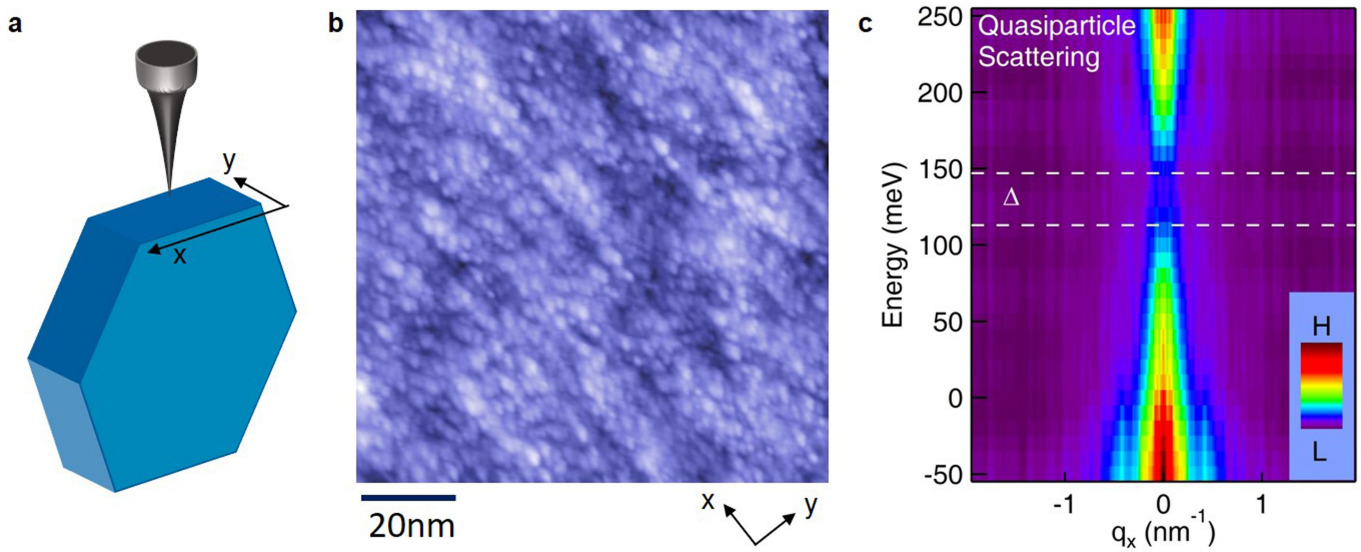

Extended Data Fig. 6 | Edge tunnelling data. a, Schematic illustrating tunnelling on the side cleaving surface. **b**, Topography of the side cleaving surface, showing stable tunnelling signal. **c**, Quasiparticle scattering along the bulk crystal edge direction (x). Substantial reduction of the scattering is observed within the Chern gap energy determined by the Landau quantization (white lines), indicating the absence of backscattering of the in-gap edge state.

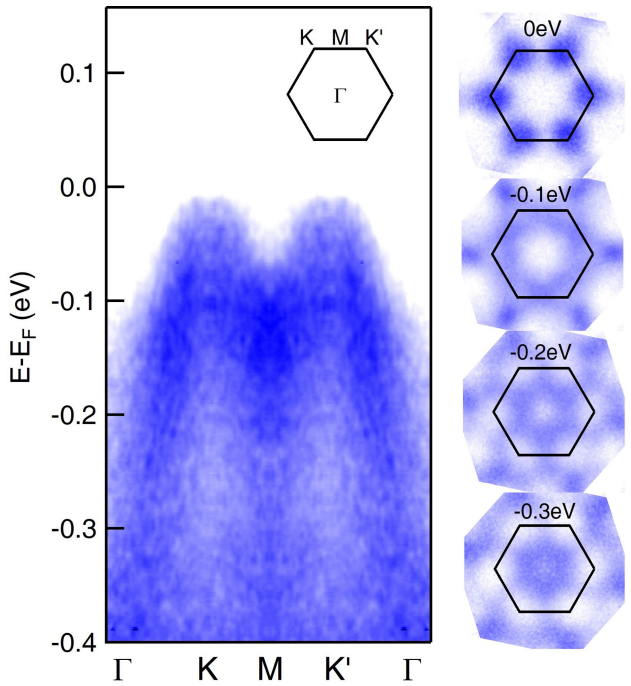

Extended Data Fig. 7 | Angle-resolved photoemission data. This set of data are taken at a phonon energy of 120 eV, showing the band dispersion along high symmetry lines (left) and the constant energy maps (right).

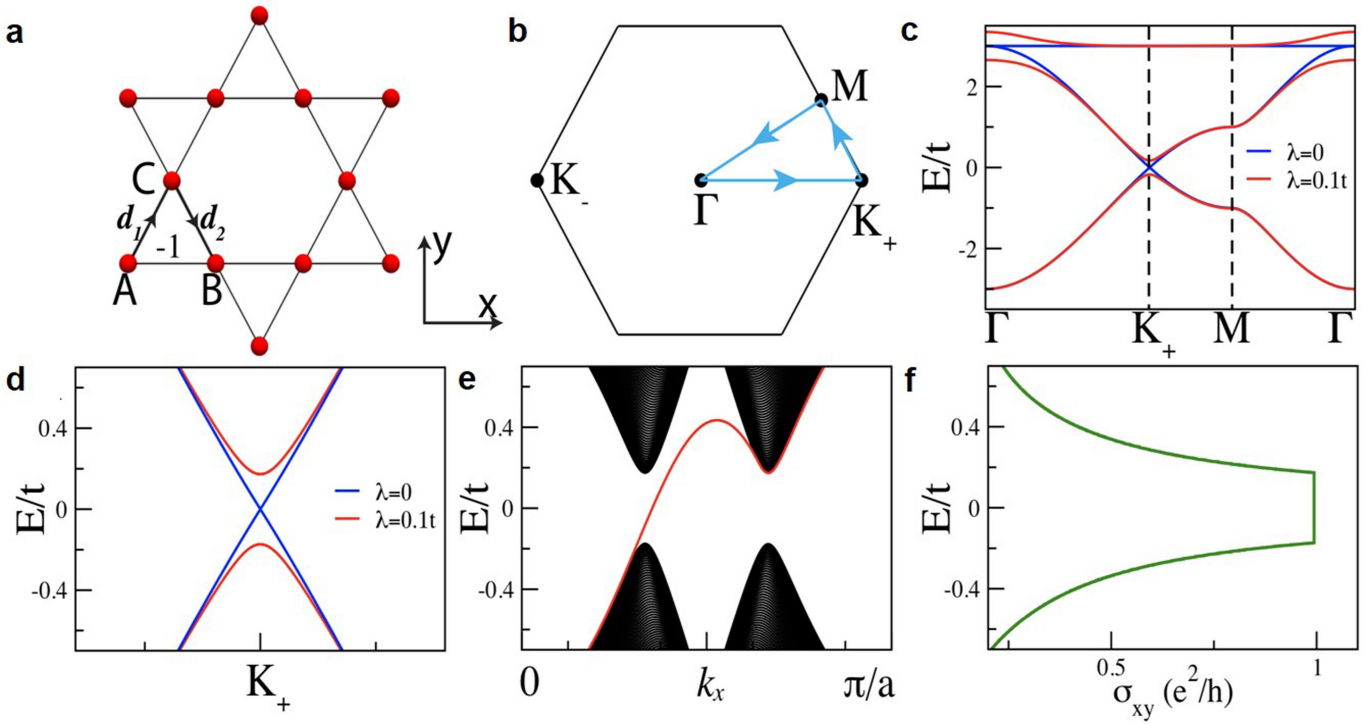

Extended Data Fig. 8 | Fundamental model for a kagome Chern magnet. **a**, The kagome lattice with the sublattice unit cell labelled by A, B and C. The Kane–Mele type spin–orbit interaction is defined with the form factor v_{ij}. **b**, The Brillouin zone of the kagome lattice with two Dirac cones at $K_{\pm} = \left(\pm\frac{2\pi}{3a}, 0\right)$. The blue path is the band structure k path used in **c**. **c**, Band structure of kagome lattice with $\lambda = 0$ (blue lines), $\lambda = 0.1t$ (red lines) and $E_D = 0$ along the k path in **b**. **d**, Band structure magnified around Dirac cone K_+. **e**, Edge states in the tight-binding model by 200 unit cells with open boundary conditions along y and periodic boundary conditions along x and $\lambda = 0.1t$ and $E_D = 0$. The red line is the edge state at the top edge. The edge state at the bottom edge is ignored here for simplicity. **f**, Hall conductivity σ_{xy} in units of e^2/h as a function of energy.

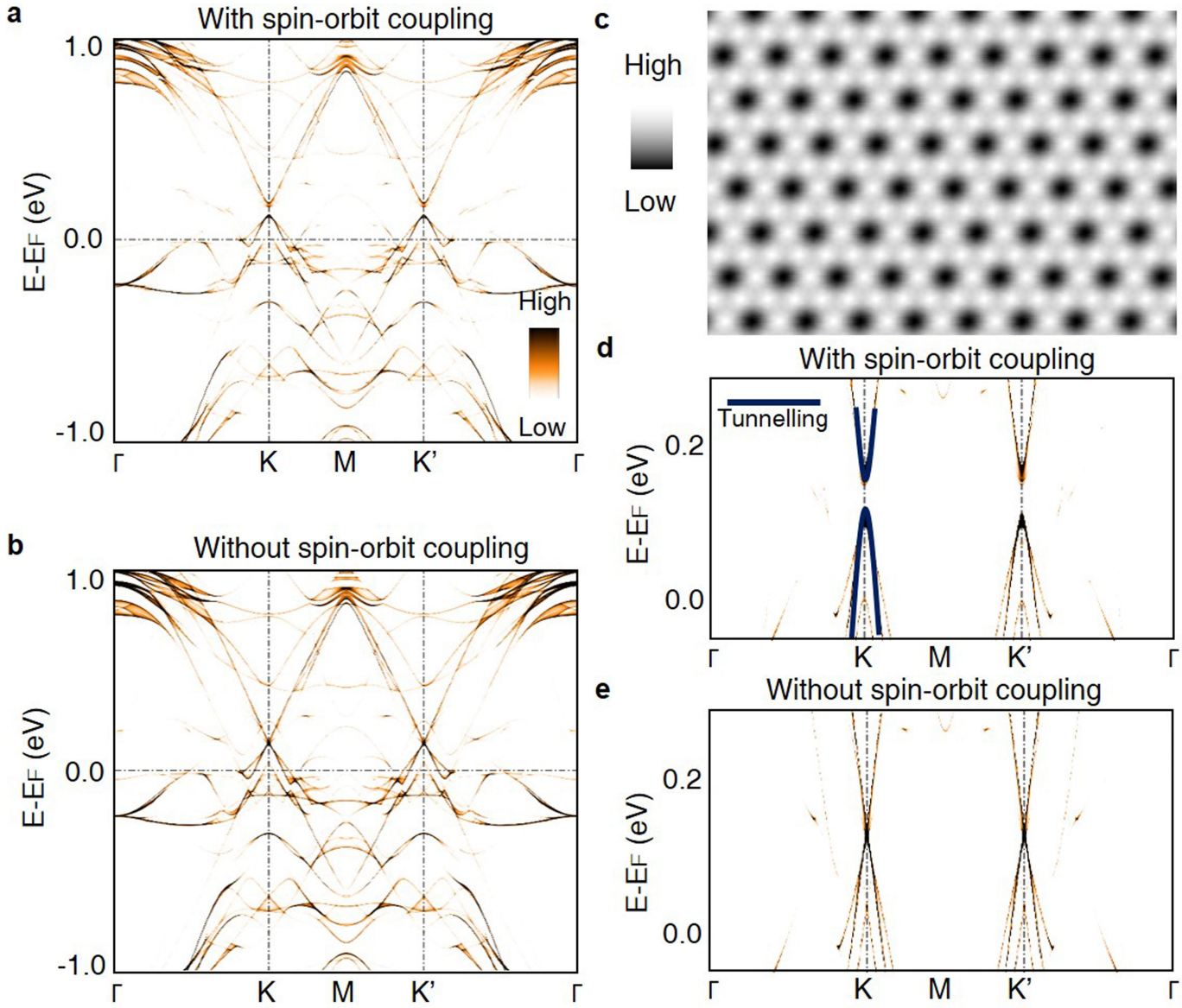

Extended Data Fig. 9 | First-principles exploration of the tunnelling signal and band structure. a, **b**, Calculated bulk band structure (momentum-resolved density of states from all orbitals along the high symmetry directions) with spin–orbit coupling (**a**) and without spin–orbit coupling (**b**). All k_z bands are projected in the surface Brillouin zone. **c**, Simulation of tunnelling topographic image of manganese kagome surface with $V = -100$ mV. **d**, **e**, Calculated manganese 3*d* in-plane orbital bands with (**d**) and without (**e**) spin–orbit coupling. The Dirac band dispersion obtained from the tunnelling data are shown as the blue curve in **d**.

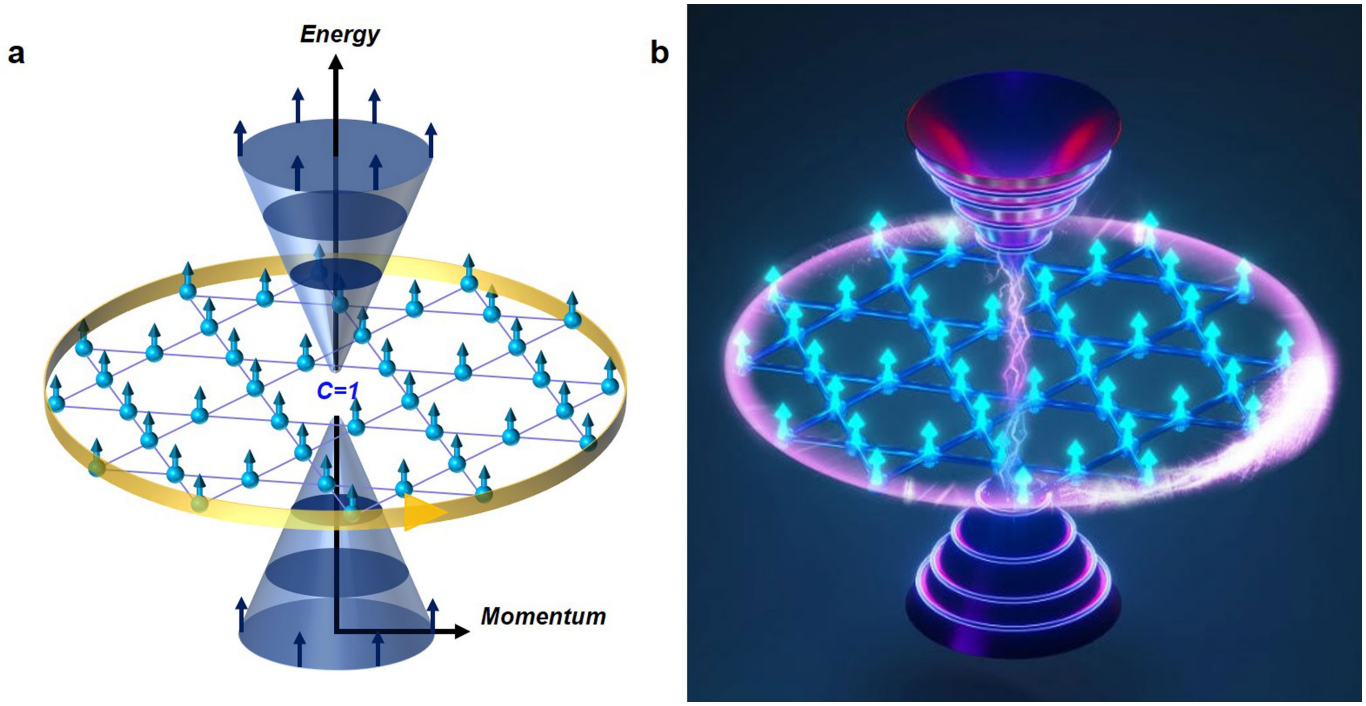

Extended Data Fig. 10 | Features of a quantum-limit Chern magnet in real space and momentum space. a, In momentum space, spin-polarized Dirac fermions with a Chern gap (two separated cones with arrows) exhibit Landau quantization where the Landau orbits are illustrated by darker area in the cones. In real space, the spin–orbit-coupled magnetic kagome lattice (spheres with arrows) carries a topological edge state (orange ring) within the Chern energy gap. The gap Chern number in this material is $C = 1$. **b**, A simplified illustration of the quantum-limit Chern magnet discovered in this work.